ACS APPLIED ENERGY MATERIALS

www.acsaem.org

Forum Article

AgBTC MOF-Mediated Approach to Synthesize Silver Nanoparticles Decorated on Reduced Graphene Oxide (rGO@Ag) for Energy Storage Applications

Arturo Barjola, Anastasia Rapeyko, Oscar Sahuquillo, Francesc X. Llabrés i Xamena,* and Enrique Giménez*

Cite This: https://doi.org/10.1021/acsaem.2c03872

Read Online

ABSTRACT: Nanowires of silver-based metal−organic framework (MOF) (AgBTC, BTC = 1,3,5-benzenetricarboxylate) were grown onto graphene oxide layers to generate GO-AgBTC nanocomposites. Thermal treatment of these composites in inert atmosphere produced reduced graphene oxide (rGO) decorated with well-dispersed and homogeneous silver nanoparticles (rGO@Ag). The easy and scalable synthesis of AgNPs via MOF-mediated synthesis was achieved by the thermal decomposition of the AgBTC directly onto the rGO surface. The structure, morphology, and electrochemical properties of this novel material were investigated by XRD, Raman, TGA, FE-SEM, TEM, cyclic voltammetry, and galvanostatic charge and discharge experimental techniques. The results showed improved capacitive features for rGO@Ag. Specific gravimetric capacitance measured by galvanostatic charge−discharge yielded a value of 151.97 F/g at the current density of 0.5 A/g, pointing out that MOF-mediated synthesis offers a facile method to generate rGO electrodes decorated by uniformly distributed nanoparticles for energy storage devices.

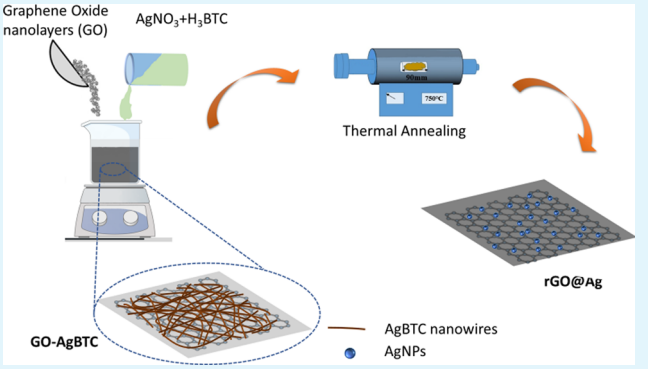

KEYWORDS: *metal−organic frameworks, graphene oxide, reduced graphene oxide, supported silver nanoparticles, energy storage*

INTRODUCTION

In recent years, many efforts have been made to overcome the current environmental problems generated by the excessive use of fossil fuels. The search for sustainable and renewable energy systems has become a priority today.[1−3]

Currently, due to their long life cycle, high power density, high capacity, and fast charge/discharge rate,[4−8] supercapacitors have emerged as an alternative or complement to other electrochemical devices such as fuel cells or batteries for storing or supplying electrical energy, mainly in systems that require high power.[4−9]

Supercapacitors can be classified as electrostatic double-layer capacitors (EDLCs) and electrochemical pseudocapacitors according to the different charge storage mechanisms.[10,11] The energy storage mechanism of EDLCs is based on a non-Faradaic process in which charges are stored electrostatically at the interfaces of electrode/electrolyte.[12] Instead pseudocapacitors store energy through a Faradaic mechanism in which charges are stored by redox reactions on the electrode surface.[9,13] Compared to EDLCs, pseudocapacitors have a greater energy density and specific capacitance, whereas EDLCs usually offer higher power density.[14−16] Electrode materials are the key factor in electrochemical device performance, so an accurate selection and optimization of them is essential to achieve functional supercapacitors.

Graphene is an excellent candidate for supercapacitor electrodes owing to its outstanding properties, such as high specific surface area,[17] superior electrical conductivity,[18] tunable porous structure,[19] and surface chemistry provided by functional groups anchored onto the graphene structure.[20,21] Various studies on supercapacitor applications of graphene-based materials have been developed, including composite graphene aerogel doped with metal oxides,[22] porous carbon,[23] conducting polymers,[24] or pristine graphene aerogels with different structural[25] or chemical modifications.[26]

Metal−organic frameworks (MOFs) are a subclass of porous coordination polymers formed by linking metal centers with organic ligands to build crystalline and porous structures.[27] Their high specific surface area and tunable size of pores[28]

Special Issue: Metal-Organic Frameworks for Energy Storage Applications

Received: December 1, 2022
Accepted: March 10, 2023

have attracted considerable attention in recent years among several research fields like gas storage and separation,[29,30] proton conducting membranes,[31,32] catalysis,[33−35] sensing,[36] or energy storage and conversion.[37] MOFs can provide the supercapacitor electrodes with pseudocapacitive redox centers. Besides, they are capable of storing charge by a non-Faradaic mechanism through their internal porosity.[38−41] The synergistic effect obtained by combining the properties of graphene with those of MOFs for supercapacitor electrode applications have already been explored,[42,43] offering promising results. In that context metal−organic frameworks supported on a graphene surface prevent the restacking of graphene sheets during the reduction process[44] as well as it provides porosity to the composite in the micropore region, where usually graphene oxide shows a poor porosity.[45] In addition, graphene oxide offers a suitable structure to accommodate the MOF crystallites and, due to their intrinsically high electronic conductivity, can also facilitate the electron transfer process at the electrode surface,[46] thus enhancing the low electrocatalytic features showed by the MOF.[47]

Alternatively, MOFs can be used as precursors of high specific surface area carbons or metal oxide materials by means of their pyrolysis or calcination.[48−50] In this sense, MOF-mediated synthesis becomes an effective and simple method to achieve high dispersion and homogeneous deposition of supported metal nanoparticles.[51]

Silver nanoparticles (AgNPs) are potential candidates to incorporate on an electrode material because of their excellent conductivity, which reduces the electrical resistivity of the electrode and improves its electron transfer rate.[52,53] In addition, the intercalation of the silver nanoparticles among the graphene oxide sheets prevents the restacking of the graphene layers during the reduction process, enhancing the electroactive surface area of the graphene-based electrode material.[54] So, different approaches have been used to prepare graphene−silver nanoparticles materials.[55−57]

Herein, a novel nanocomposite based on a silver—metal−organic framework (Ag-BTC) grown onto graphene oxide surface was thermally treated in order to generate a reduced graphene oxide decorated with silver nanoparticles (rGO@Ag) via MOF-mediated synthesis.

2. EXPERIMENTAL PART

2.1. Materials. All of the chemicals were reagent grade (Alfa Aesar, Sigma-Aldrich, Valencia, Spain) and used as received.

2.2. GO Synthesis. GO was synthesized from natural graphite by means of the improved Hummer's method.[58] Concentrated H_2SO_4 and concentrated H_3PO_4 were mixed in a 9:1 (v:v) proportion. Next, this solution was added to graphite powder and $KMnO_4$ (1:6 (wt %)) in an ice bath and then stirred for 12 h at 50 °C. Then, it was cooled to room temperature and poured into an ice water with H_2O_2 (30%). The mixture was sifted through a testing sieve (250 μm) and recovered by centrifugation (4000 rpm for 4 h), discarding the supernatant. The centrifugated solid was then rinsed twice with 200 mL of water, 200 mL of 30% HCl, and 200 mL of ethanol. Finally, the remaining material was coagulated with 200 mL of ether and filtered through a 0.45 μm pore size membrane. The product obtained was collected with deionized water and subsequently dried by lyophilization.

2.3. MOF Synthesis. AgBTC MOF was prepared using a "green" aqueous synthesis procedure described by Nowacka et al.[59] with slight modifications. Briefly, 20 mL of aqueous solution of 0.1 M Na_3BTC (trisodium-1,3,5-benzenetricarboxylate) was added to silver nitrate (3 mmol) under vigorous stirring with a magnetic stirrer. After that, 10 mL of ethanol was added to promote precipitation. The mixture was left stirring at ambient temperature for 15 min. The obtained white solid was recovered by centrifugation and washed with Milli-Q water and ethanol. Finally, the resulting powdered material was dried at ambient temperature during 24 h under dark conditions.

2.4. GO-MOF Nanocomposite Synthesis. GO-AgBTC nanocomposites with different GO-Ag^+ ratios were prepared according to the following procedure (exemplified for a 5:1 ratio): 0.1 mL of aqueous $AgNO_3$ solution (37.8 mg/mL) was added dropwise to 24 mL of aqueous GO dispersion (0.5 mg/mL) under vigorous magnetic stirring. Subsequently, 0.15 mL of 0.1 M Na_3BTC aqueous solution and 0.075 mL of ethanol were added dropwise, thus affording the formation of AgBTC in situ. Then, the mixture was left for 15 min under stirring at ambient temperature. Finally, the resulting material was dried by lyophilization to obtain powdered GO-AgBTC nanocomposite. In this way, three composites were prepared with GO-Ag^+ weight ratios of 0.5:1, 1:1, and 5:1.

2.5. rGO@Ag Synthesis. rGO@Ag was prepared from GO-AgBTC by thermal treatment. An amount of 39.68 mg of GO-AgBTC 5:1 was placed in an alumina crucible and subjected to 600 °C for 2 h in a tube furnace, with a heating rate of 5 °C/min under a nitrogen atmosphere. The obtained material was thoroughly washed with deionized water and dried at 80 °C for 24 h in an oven.

2.6. Characterization. X-ray powder diffraction (XRD) measurements were performed with Cu Kα radiation on either a Panalytic Cubix'Pro diffractometer or a Bruker D2 Phaser instrument. Thermogravimetric analyses (TGA) were performed on a TA Instruments TGA Q50 analyzer. Samples (5−10 mg) were weighed in titanium crucibles and heated under nitrogen atmosphere from 50 to 800 °C at a heating rate of 10 °C min^{-1}. The surface morphologies were obtained by field emission scanning electron microscope (FE-SEM), a Zeiss, Ultra 55 instrument equipped with energy dispersive X-ray spectrometer (EDS, Oxford Instruments) for elemental composition measurements. The structure and composition of the samples were studied by X-ray photoelectron spectroscopy (XPS) with a Thermo Fisher Scientific VG-Microtech Multilab 3000 photoelectron spectrometer. Raman spectroscopy studies were performed on a Xplora spectroscope using a 532 nm laser (Horiba). Electrochemical measurements were performed in an Autolab PGSTAT 302 (ECO-CHEMIE) potentiostat at room temperature. A typical three-electrodes cell was used to evaluate the electrochemical properties of the different materials. Ag/AgCl (3 M KCl) electrode and a platinum foil were employed as the reference and counter electrodes, respectively. A mixture of active material, conductive carbon black Super P (99+%), and poly(vinylidene fluoride) (PVDF) binder in the weight ratio of (80:10:10) were diluted in a certain amount of *N*-methylpyrrolidone (NMP) to achieve a homogeneous dispersion of 1 mg/mL. Then, the mixture was drop-cast onto a stainless-steel electrode with an active material mass loading of 0.08 mg/cm^2. As-prepared electrodes were dried at 80 °C overnight in an oven.

Cyclic voltammograms (CVs) were obtained at different scan rates (2−200 mV/s). The specific capacitance, C_s (F/g), was calculated by eq 1:

$$C_s = \frac{\int I \, dV}{2vm\Delta V} \tag{1}$$

where $\int I \, dV$ is the area bounded by the CV curves, m represents the mass of active material, v is the scan rate, and ΔV is the potential range employed in the measurement.

Galvanostatic charge−discharge (GCD) curves were recorded at the current densities of 0.5, 1, 2, and 5 A/g, and gravimetric specific capacitance was obtained by eq 2:

$$C_s = \frac{I\Delta t}{m\Delta V} \tag{2}$$

where I and t are the discharge current and the discharge time, respectively. The mass of active material is m, and ΔV is the voltage range of the measurement.

https://doi.org/10.1021/acsaem.2c03872
ACS Appl. Energy Mater. XXXX, XXX, XXX−XXX

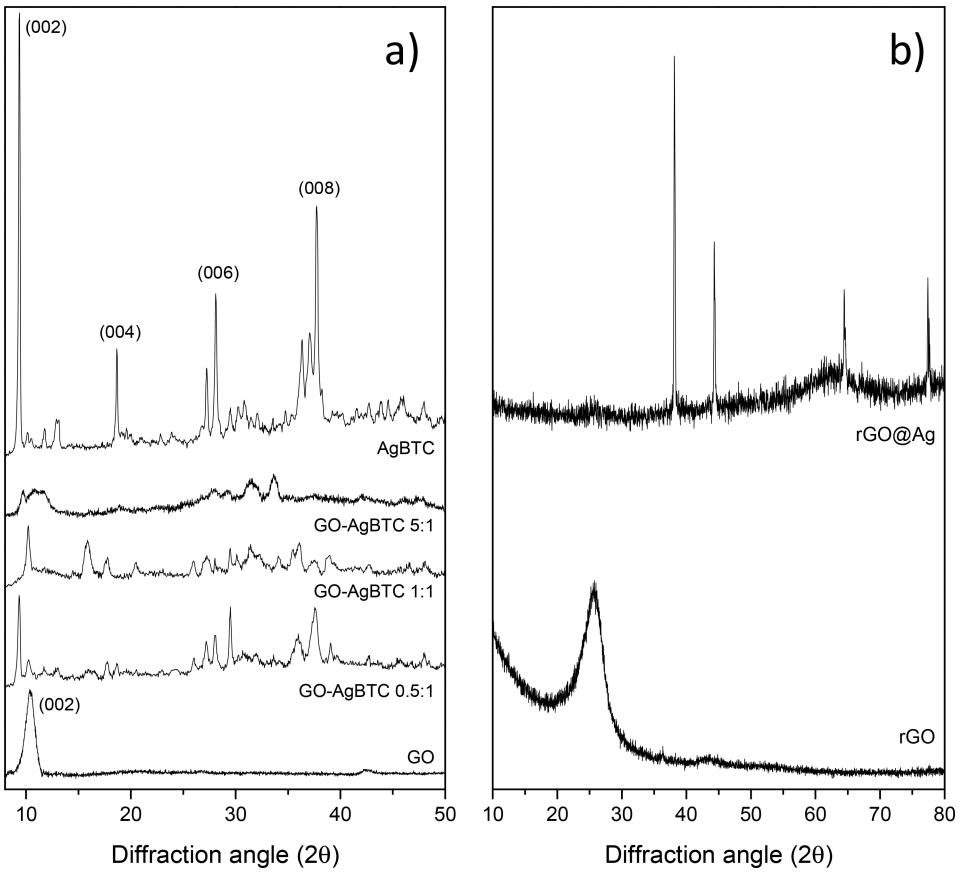

Figure 1. XRD patterns (Cu Kα radiation) of (a) GO, AgBTC, and GO-AgBTC nanocomposites with GO-Ag^+ ratios of 0.5:1, 1:1, and 5:1 and (b) rGO and rGO@Ag.

3. RESULTS AND DISCUSSION

3.1. Synthesis of GO-AgBTC Composites. GO-AgBTC nanocomposites with different GO-Ag^+ ratios, prepared as described in the Experimental Part, were first characterized by XRD and electron microscopy.

The presence of a sharp diffraction peak at $2\theta = 10.3°$ in the XRD pattern of GO (Figure 1a, bottom line), assigned to the (002) planes, reflects the good grade of oxidation achieved with the chemical process employed to convert the graphite precursor to graphene oxide.

The XRD pattern of as-synthesized AgBTC (Figure 1a, top line) is analogous to the phase previously described by Morris et al.,[60] although some minor additional peaks are also visible in our diffractogram, most likely belonging to AgBTC compounds with different structure (as also described in the work by Morris et al.[60]). According to the single-crystal X-ray analysis reported by Morris' group, this MOF crystallizes in the triclinic space group, $P\bar{1}$. The asymmetric unit contains 14 Ag^+ ions, four molecules of BTC, and two hydroxyl groups, giving an overall chemical formula of $Ag_{14}(C_9H_3O_6)_4(OH)_2$. This structure can be described as infinite zigzag chains of Ag^+ clusters running along the *b*-axis and connected by trimesate anions forming a three-dimensional framework with small pores along the *a*-axis. The FE-SEM images of AgBTC and GO-AgBTC nanocomposites are shown in Figure 2. It can be observed that AgBTC crystallizes in the form of large, micrometer sized plates, which tend to break down into rods and, eventually, into thin long wires (see Figure 2).

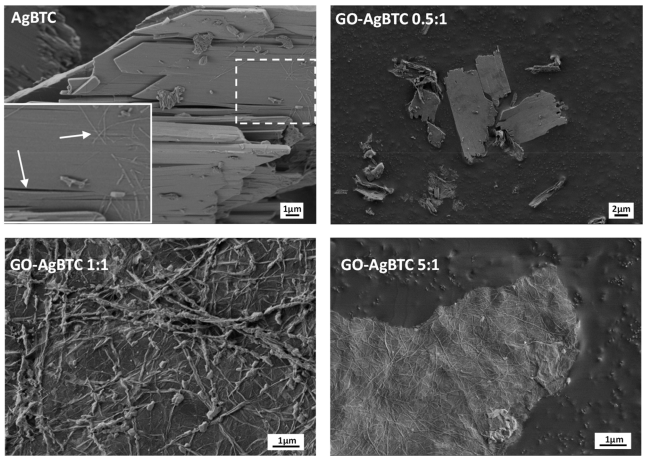

Figure 2. FE-SEM images of AgBTC and GO_AgBTC composites with 0.5:1, 1:1, and 5:1 GO-Ag^+ ratios. The inset in the image of AgBTC evidences the presence of some individual nanowires, as well as the tendency of the plates to break down lengthwise (indicated by an arrow).

When AgBTC was prepared in situ in the presence of GO, the morphology of the MOF changed drastically, depending on the GO-Ag^+ ratio used. When a 1:1 ratio was used, the large AgBTC plate crystals observed for the parent MOFs were no longer formed, but AgBTC tended to crystallize into thick bundles of nanowires decorating the whole surface of the GO, along with a small fraction of small flake crystals (Figure 2). This clearly indicates that the presence of GO during the MOF

https://doi.org/10.1021/acsaem.2c03872
ACS Appl. Energy Mater. XXXX, XXX, XXX−XXX

synthesis largely prevents the formation of plate crystals by the aggregation of the wires into three dimensions. Thus, in sample 1:1 GO-AgBTC, GO becomes a support onto which AgBTC nanowires are dispersed. Accordingly, important changes are also observed in the XRD pattern of 1:1 GO-AgBTC with respect to the parent MOF. In the diffractogram of pure AgBTC, main peaks are observed at 2θ = 9.36°, 18.67°, 28.1°, and 37.7°. These peaks correspond to planes (0 0 2), (0 0 4), (0 0 6), and (0 0 8), respectively, which are parallel to the faces of the plate crystals. Their relative intensities are high due to preferred orientation during the acquisition of the powder XRD. This phenomenon results from a nonrandom orientation of the crystals when the powder is compacted in the X-ray sample holder, which tends to be oriented preferentially in the crystallographic direction corresponding to the extended flat faces. In the case of AgBTC, this preferred orientation produces an increase of the relative intensities of planes with Miller indices (0 0 2l). However, these peaks almost disappear in the XRD pattern of 1:1 GO-AgBTC, which reflects the change of morphology from plates to nanowires, which now produce a different preferred orientation, exposing preferentially the planes with Miller indices (h h 0); i.e., peak (1 1 0) at 10.2° 2θ in the diffractogram of sample 1:1 GO-AgBTC. When the amount of GO in the composite is further increased to a GO-Ag^+ ratio of 5:1, these AgBTC nanowires decorating the GO surface become much thinner (Figure 2), while the XRD pattern is largely dominated by a broad peak at ca. 10−15° 2θ due the GO support. The intensities of the diffraction peaks associated with the AgBTC MOF are much lower (worse signal-to-noise ratio) than in sample GO-AgBTC 1:1 due to the lower content of the Ag MOF in the composite, but they can still be clearly distinguished in the diffractogram as broad bands. The presence of these diffraction peaks demonstrates that the same (or a similar) MOF structure is formed also in the most diluted sample, which is supported by the fact that the same nanowires morphology is observed for both 1:1 GO-AgBTC and 5:1 GO-AgBTC samples. Conversely, when the GO-Ag^+ ratio in the composite decreases to 0.5:1, GO is no longer able to exert the role of support for the MOF nanowires. Therefore, large AgBTC plate crystals similar to those in the pure material are formed in 0.5:1 GO-AgBTC, so the XRD patterns are also very similar, with only small variations of relative intensities of some peaks. Note also that in none of the GO-AgBTC samples it is observed the presence of diffraction peaks at ca. 38° 2θ, which would reflect the presence of metallic silver nanoparticles.

It is therefore clear that the GO-Ag^+ ratio is a key controlling factor determining the morphology of AgBTC crystals in the composite system. According to our XRD and electron microscopy analyses, the lowest limit to obtain well-dispersed AgBTC wires wetting the GO surface is a 1:1 GO-Ag^+ ratio, although a 5:1 ratio affords thinner wires and better dispersions of the MOF. Therefore, we selected the GO-AgBTC 5:1 composite to carry out further studies, as described below.

3.2. Preparation of rGO@Ag Composite by Thermal Reduction. Upon thermal reduction of pure GO, the diffraction peak initially displayed at 10.3° 2θ is shifted to 22.3° (Figure 1b) and broaden for the rGO material. As a consequence of the restoration of graphitic structure due to the reduction of the functional oxygen groups on the material surface during the thermal treatment applied, restacking of the material is also promoted during the reduction process, decreasing the intersheet distance from 0.86 nm obtained for GO to 0.35 nm calculated for rGO.

In the case of 5:1 GO-AgBTC, thermal reduction brings about dramatic chemical and morphologic changes, which are associated with the reduction of the GO support accompanied by the decomposition of the AgBTC nanowires to generate silver nanoparticles (AgNPs). Prominent, sharp diffraction peaks are observed at 2θ = 38.1°, 44.3°, 64.5°, and 77.5°, corresponding to crystallographic planes of face-centered cubic (fcc) AgNPs (1 1 1), (2 0 0), (2 2 0), and (3 1 1), respectively [JCPDS Card No. 07-0783]. Therefore, this composite will be hereafter referred to as rGO@Ag, which reflects the chemical changes undergone during the thermal reduction process on both the support and the silver MOF.

Raman spectra of GO, rGO and rGO@Ag compounds were further employed to analyze the structural changes in the GO-based materials promoted by the thermal treatment and to study the graphitization degree of the graphene oxide materials (see Figure 3). Characteristic bands around 1345 and 1579

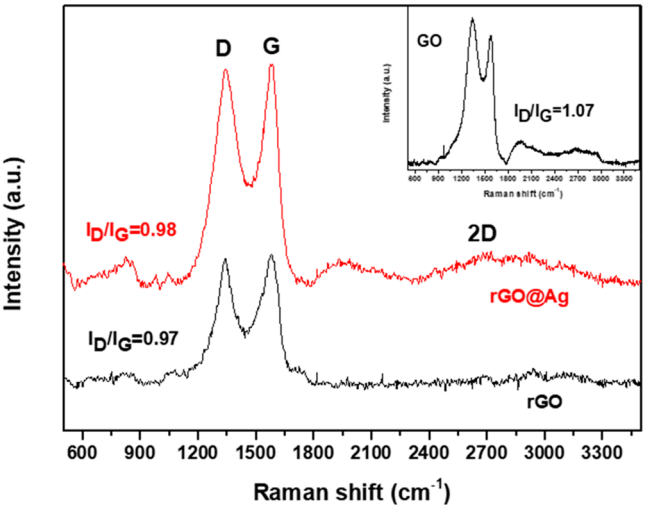

Figure 3. Raman spectra of rGO (black), rGO@Ag (red), and GO (inset).

cm^{-1} associated with D and G first order modes in graphene compounds were found in all cases, together with additional broader second order modes assigned to 2D (2690 cm^{-1}) and D + G combination band (2924 cm^{-1}).[61] Raman spectroscopy can be used to study the graphitization degree of graphene oxide materials. The D band is caused by the sp^3 carbon atoms vibrations and is related with defects introduced in the material. Conversely, G band is due to the stretching vibrations of the sp^2 carbon atoms present in the hexagonal graphite domains. The ratio between the intensities of the D and G band (I_D/I_G) is a useful parameter to evaluate the crystallinity grade of the sample.[62] The values obtained for GO, rGO, and rGO@Ag were 1.07, 0.97, and 0.98, respectively. The lower values obtained for rGO and rGO@Ag compared to the value obtained for GO indicate the partial recovery of the graphitic order after the thermal treatment is carried out. Moreover, there is not significant difference among the values obtained for rGO and rGO@Ag, indicating the predominant effect of the thermal treatment on the structure of the material compared to the effect produced by its decoration with the silver nanoparticles obtained from the decomposition of the AgBTC MOF. This fact also suggests that no covalent bonds

https://doi.org/10.1021/acsaem.2c03872
ACS Appl. Energy Mater. XXXX, XXX, XXX−XXX

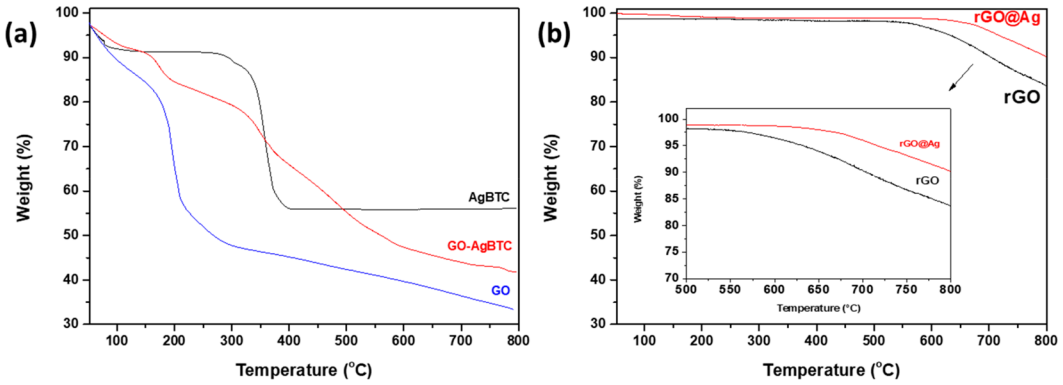

Figure 4. TGA curves of the different materials before (a) and after (b) thermal treatment.

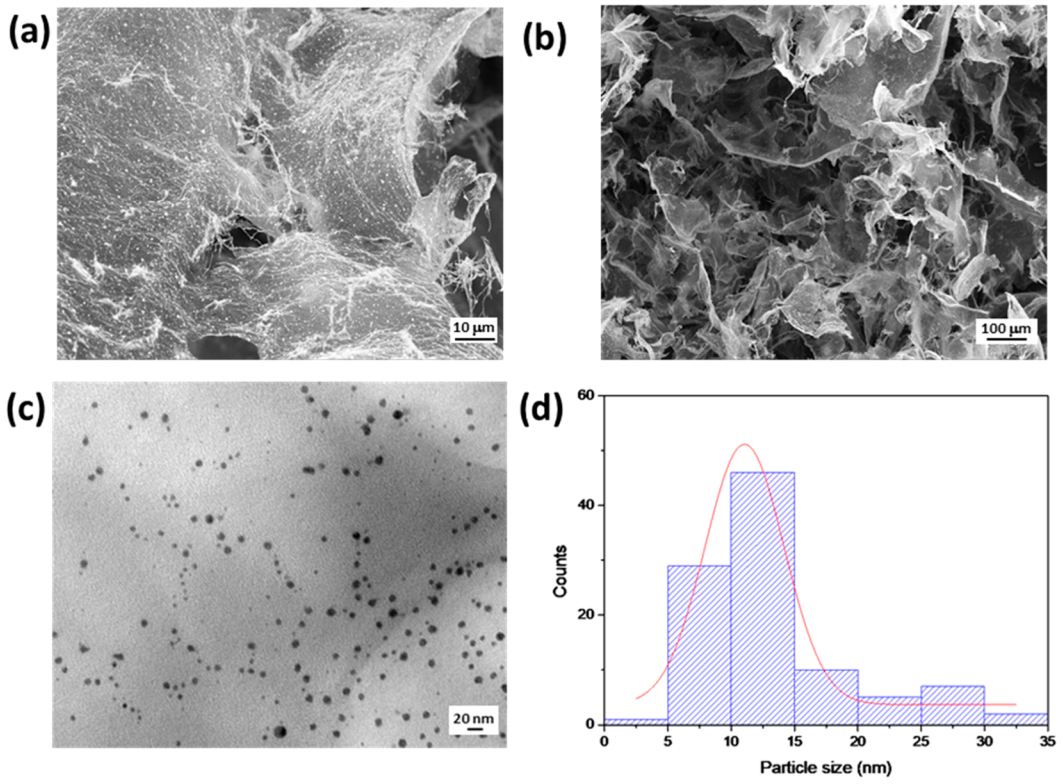

Figure 5. FE-SEM images at different magnifications (a, b), and TEM micrograph (c) of rGO@Ag. (d) AgNPs particle size histogram obtained from the TEM analysis.

exist between the graphene surface and the deposited AgNPs, but they should rather interact by weak van der Waal forces.[63]

Thermogravimetric analysis was conducted to evaluate the thermal properties of the materials studied. Samples (5−10 mg) were heated under nitrogen atmosphere from 50 to 800 °C at a heating rate of 10 °C min^{-1}. GO-based compounds present three stages of mass loss. (Figure 4a). The first one occurs at temperatures under 150 °C, and it is related with the evaporation of the adsorbed and structural water.[64] The second weight loss, between 200 and 300 °C, is associated with the decomposition of the more labile oxygen-containing functional groups attached to the material structure.[65] Above this point, the more stable oxygen functionalities were removed.[66] AgBTC presents a slight loss weight at temperatures below 100 °C due to the elimination of the adsorbed water on its surface and a pronounced step around 324 °C related with the decomposition of the MOF structure. Concerning the 5:1 GO-AgBTC composite, the TG curve shows higher thermal stability compared with pure GO, with an additional weight loss in the range of 324 and 600 °C caused by the presence of AgBTC in the material. The TG curves obtained for both materials after the reduction process (Figure 4b) confirm the restoration of the original graphitic order. There is not significant mass loss up to temperatures above 540 °C for rGO and 595 °C for rGO@Ag. These results support the success of the reduction process as well as the improvement effect on the thermal properties of the rGO material achieved by the thermal decomposition of the AgBTC precursor onto the rGO surface providing rGO@Ag with a uniformly dispersed thermally stable layer of carbon-AgNPs[67,68] coming from the carbonization of the organic

https://doi.org/10.1021/acsaem.2c03872
ACS Appl. Energy Mater. XXXX, XXX, XXX−XXX

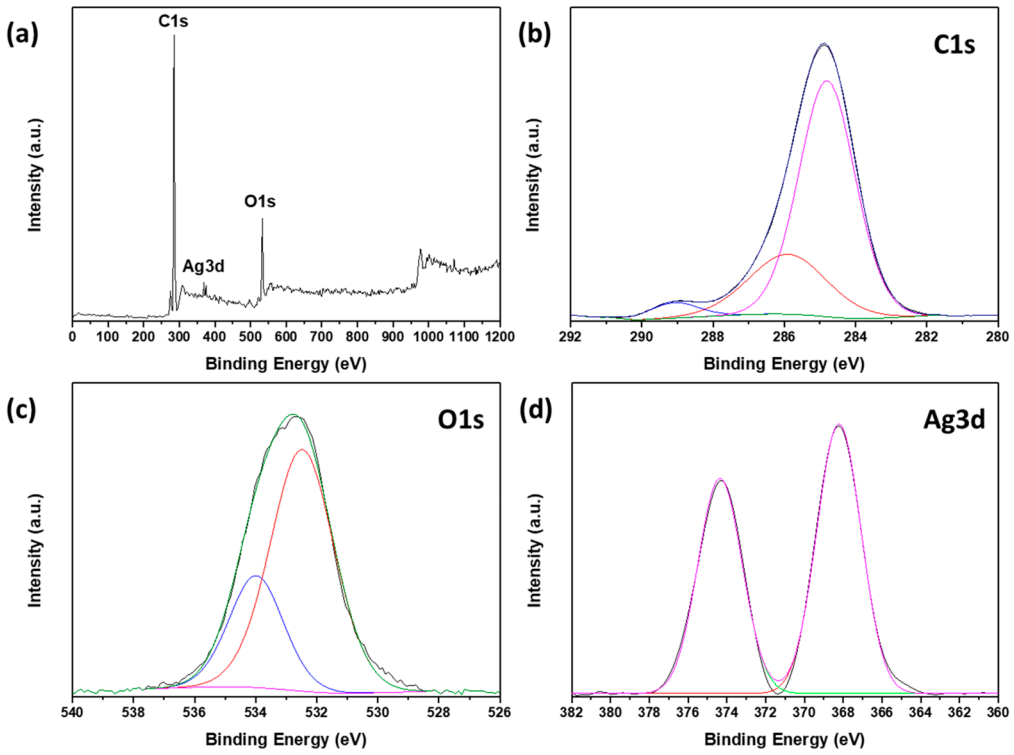

Figure 6. XPS spectra of rGO@Ag: (a) survey, (b) C 1s, (c) O 1s, and (d) Ag 3d.

ligand of the MOF as well as from the reduction of inorganic silver nodes which generate silver nanoparticles on its surface.

Figure 5 shows FE-SEM micrographs corresponding to the reduced material, rGO@Ag, with different magnifications. Uniformly distributed AgNPs provided by the decomposition of AgBTC nanowires decorate the rGO sheets in the porous structure of the rGO@Ag material. Color mapping shown in Supporting Information Figure S1a reveals the distribution of the C, O, and Ag on the rGO@Ag sheets. Transmission electron microscopy was further employed to evaluate the shape and distribution of the resulting AgNPs obtained upon thermal decomposition of the AgBTC MOF. According to the TEM micrographs and histogram shown in Figure 5c,d, rGO@Ag displays homogeneous and well-dispersed sphere-like silver nanoparticles with a mean size around 10 nm covering the rGO sheets. A small fraction of larger particles (about 5% of the total; see Figure S1b) are also present in the sample, which would be responsible for the narrowing of the XRD peaks in Figure 1b (mean particle size calculated with the Scherrer equation is 35−40 nm). Interestingly, the stabilizing role of the GO support and the capping effect of the benzene tricarboxylic acid linker of the MOF largely prevent the formation of micrometer sized silver nanoparticles aggregates. The excellent dispersion of the AgNPs achieved on the rGO surface is clearly a consequence of the formation of well-defined thin fibers of the AgBTC precursor, thus evidencing the importance of controlling the morphology of the MOF by properly selecting the GO-Ag^+ ratio used during the synthesis of the composites.

Finally, XPS analysis was used to characterize the evolution of the surface composition of materials throughout the synthesis process. Deconvolution of the C 1s spectra for graphene oxide (Figure S2b) depicts several peaks at 284.60, 285.12, 286.84, and 288.49 eV, attributed to the C−C/C═C, C−O, C−O−C, and O−C═O groups, respectively.[69] The intensity of the C═C peak increased upon the GO-AgBTC synthesis due to the presence of the BTC linker used to generate the MOF (Figure S3b). However, the intensity of other peaks corresponding to carbon oxygenated groups of GO material was practically unchanged after incorporation of AgBTC. (Figure S3b). Moreover, signals at 368.3 and 374.3 eV corresponding to Ag $3d_{3/2}$ and Ag $3d_{5/2}$ (Figure S3a,d)[70] were also detected in GO-AgBTC nanocomposite. These results confirm the successful AgBTC formation onto the GO surface.

The XPS spectra of rGO are presented in Figure S4. In the C 1s region, a great decrease of intensity of peaks associated with carbon oxygenated groups was observed, indicating successful reduction of graphene oxide (Figure S4a,b) The results obtained for rGO@Ag survey spectra (Figure 6a) confirm the presence of silver in the material, and the relative intensity ratio between C 1s and O 1s peaks suggest the high degree of reduction achieved upon the thermal treatment employed. C 1s spectra of rGO@Ag (Figure 6b) reflect results similar to those of rGO with a prominent peak associated with C═C and a weak presence of the bands corresponding to oxygenated groups. Peaks at 368.2 and 374.3 eV attributed to Ag $3d_{3/2}$ and Ag $3d_{5/2}$ were assigned to metallic silver. These results confirmed the successful reduction of GO-AgBTC nanocomposite by pyrolysis under N_2 atmosphere, generating reduced graphene oxide decorated with silver nanoparticles rGO@Ag.

3.3. Electrochemical Properties. The electrochemical properties of AgBTC, GO, GO-AgBTC, rGO, and rGO@Ag were analyzed by cyclic voltammetry using the three-electrode configuration in 1 M Na_2SO_4 aqueous electrolyte in the potential window that ranged from −1 to 0 V versus Ag/AgCl, where silver nanoparticles were stable from oxidation reactions (Figure S6). First, we confirmed that both AgBTC and GO-AgBTC samples were stable under the aqueous electrolyte solution used for electrochemical measurements (see Figure S6e). Subsequently, a more complete study including charge−

https://doi.org/10.1021/acsaem.2c03872
ACS Appl. Energy Mater. XXXX, XXX, XXX−XXX

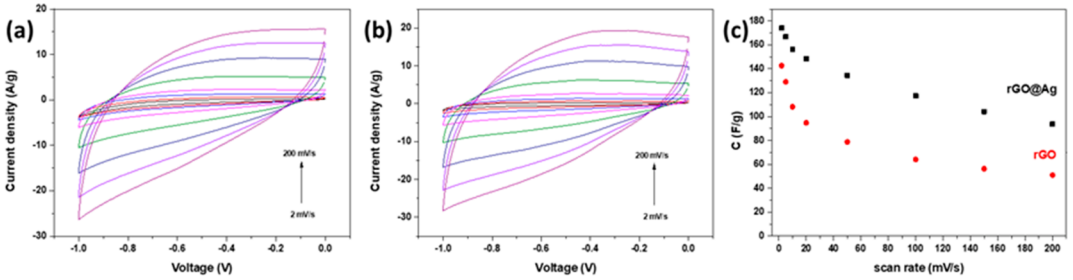

Figure 7. Cyclic voltammetry curves at different scan rates from 2 to 200 mV/s for rGO (a) and rGO@Ag (b). Specific gravimetric capacitance values obtained from the voltametric curves at the different scan rates measured (c).

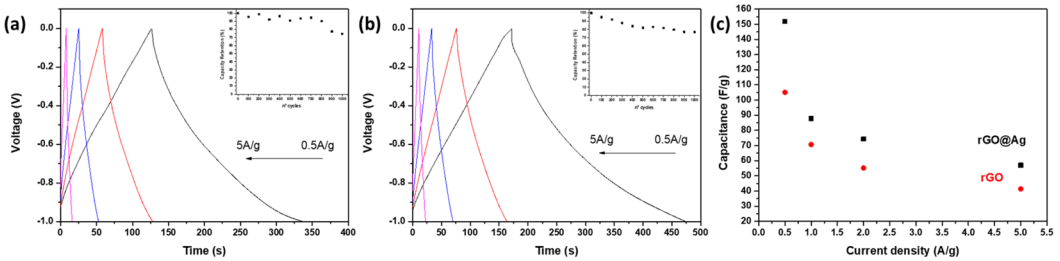

Figure 8. Charge−discharge measurements at 0.5, 1, 2, and 5 A/g current densities for rGO (a) and rGO@Ag (b). Capacity retention at 1000 cycles (insets) for rGO (a) and rGO@Ag (b). Specific gravimetric capacitance values obtained from galvanostatic charge−discharge curves at different current densities measured for rGO@Ag (black squares) and rGO (red circles) (c).

discharge curves were performed for the rGO and rGO@Ag materials, which provided better specific gravimetric capacitance values from the cyclic voltammetry results. Figure S6 depicts the voltametric curves measured for GO, AgBTC, and GOAgBTC. The charge enclosed in the CV curves increase along with the increasing of the scan rate for all materials studied. Moreover, GO (Figure S6a) presents a distorted rectangle shape without any redox peaks, suggesting the typical double layer capacitive charge storage mechanism.[71] Otherwise, AgBTC (Figure S6b) shows several peaks in the anodic and cathodic sweeps associated with a pseudocapacitive charge storage mechanism provided to the redox centers present in the material.[72] In the case of GO-AgBTC (Figure S6c), the voltametric curves showed features from both GO and AgBTC behavior. Plots of the specific capacitance calculated from the voltametric curves as a function of the scan rate are depicted in Figure S6d. Capacitance values are lower for the unreduced materials, as was expected due to their lack of conductivity. For AgBTC and GO-AgBTC, the values are slightly higher than those of GO, probably due to the pseudocapacitive effect provided by AgBTC. In addition, better results obtained for AgBTC-based materials suggest that their porosities are more accessible than that of GO. Note that when the scan rate is very low (2 mV/s) and the charge storage mechanism is not limited by the diffusion process, the capacitance value of GO exceeds those of AgBTC and GO-AgBTC. However, when the scan rate increases above 2 mV/s, capacitance values of GO suffer a pronounced fall due to diffusion limitations.

Figures 7 and S7 show cyclic voltammetry curves for rGO (a) and rGO@Ag (b). The charges enclosed by the voltammetric curves decrease when the scan rate increases from 2 to 200 mV/s. Specific gravimetric capacitance values obtained by eq 1 for rGO@Ag and rGO are plotted against the scan rate (ν) in Figure 7c. The specific gravimetric capacitance decreases when the scan rate increases since, at low scan rates, both internal and external surface porosity of the sample can take part in the charge storage mechanism, while at high scan rates only the external surface porosity of the electrode is disposable to the charge transfer process. rGO@Ag displayed values above those of rGO for the range of all scan rates studied, yielding the best value of 174.11 F/g at 2 mV/s, compared with a best value of 142.65 F/g obtained for rGO. Thus, the enhancement of the charge storage capacity achieved with the incorporation of the silver nanoparticles onto the GO-based material is remarkable.

Charge−discharge curves for both materials were also recorded (Figure 8), and specific gravimetric capacitances were calculated by eq 2 at different current densities of 0.5, 1, 2, and 5 A/g in the voltage range from 0.00 to −1.00 V. As it can be observed in Figure 8, when the current density was increased, the specific gravimetric capacitance was decreased for both materials. However, the values obtained for rGO@Ag were higher than those obtained for rGO at all current densities. The best value of 151.97 F/g was achieved for rGO@Ag at 0.5 A/g versus 105.30 F/g reached for rGO at the same current density. A comparison of the specific capacitance obtained for rGO@Ag composite with other reported rGO-Ag-based materials is summarized in Table S1, showing the good performance achieved for the synthesized rGO@Ag material as supercapacitor electrode. Capacity retention at 1000 cycles was evaluated at the current density of 5 A/g (Figure 8 insets in parts a and b). rGO@Ag showed a capacity retention of 77.08% with a more pronounced decrease of its retention at the first 400 cycles. Meanwhile, rGO presents a lower capacity retention of 74.48% at 1000 cycles but it could maintain an excellent retention capacity of 90.01% up to 800 cycles

To understand the charge storage mechanism of these materials, a Trasatti's analysis[73] was carried out for rGO@Ag and rGO. The total charge stored in an electrode (q_t) can be expressed as a sum of two contributions. The charge stored by its inner surface (q_i), which depends on the diffusion of the species in the electrode, and the charge stored by the outer surface (q_0) of the electrode, which depends on the scan rate and is not limited by the diffusion process.

https://doi.org/10.1021/acsaem.2c03872
ACS Appl. Energy Mater. XXXX, XXX, XXX−XXX

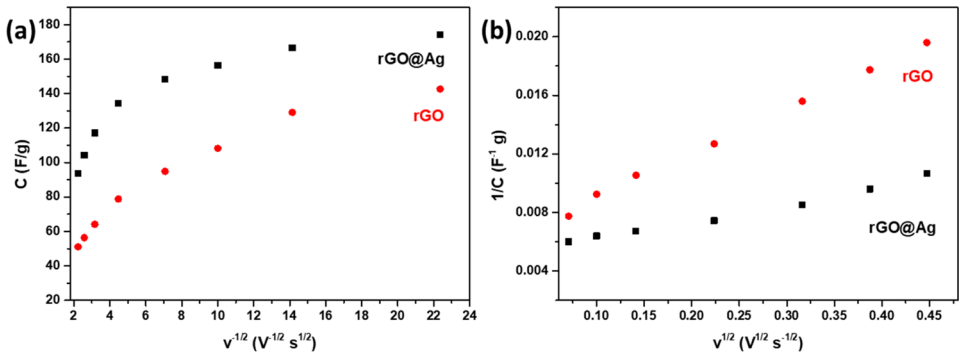

Figure 9. Dependence of the specific gravimetric capacitance for rGO and rGO@Ag versus the reciprocal of the $v^{-1/2}$(a) and the reciprocal of the specific gravimetric capacitance for rGO and rGO@Ag versus $v^{-1/2}$(b).

$$q_t = q_0 + q_i \quad (3)$$

So, a higher value of q_0 is related with a faster ion charge transfer kinetics and a more accessible surface porosity.

The total charge stored for the electrode can be expressed as a function of the scan rate used in a cyclic voltammetry measurement (v) by eq 4:

$$q_t = q_0 + kv^{1/2} \quad (4)$$

where k is a constant value determined from the slope of the plot.

Figure 9a depicts the specific gravimetric capacitance of rGO@Ag and rGO materials plotted versus $v^{-1/2}$. Different slopes can be distinguished in this graph, which are associated with different scan rate regions. When the scan rate is below 50 mV/s, the charge storage mechanism is not controlled by diffusion since ions have enough time to access the inner porosity of the sample. Therefore, external charge transfer dominates the charge storage mechanism. Otherwise, when the scan rate is above 50 mV/s, the ions have no time to reach all of the inner pores of the sample. In this case, the charge storage mechanism is controlled by the ions diffusion in the sample.[74,75] Then, the value of q_0 in eq 4 can be obtained from the linear extrapolation of the q_t plot versus $v^{-1/2}$ in this range of scan rates when the $v^{-1/2}$ tends to infinite. On the other hand, from the plot of the reciprocal of q_t versus $v^{1/2}$ shown in Figure 9b, the value of q_t can be obtained by the linear extrapolation when $v^{1/2}$ tends to zero. The value of the q_0/q_t is a useful index to evaluate the contribution to the total capacitance from the external surface of the sample. Values of 45.24 and 73.66% were calculated for rGO and rGO@Ag, respectively, pointing out to the superior ion accessible surface for rGO@Ag with respect to rGO.

4. CONCLUSIONS

Herein we have described a method for the in situ synthesis of silver-containing AgBTC MOF in the presence of GO. We have found that the GO-Ag^+ ratio used is of paramount importance to determine the morphology of the resulting MOF crystallites. In particular, by adopting a GO-Ag^+ ratio of at least 1:1, or preferably 5:1, it is possible to prepare GO-AgBTC composites in which the MOF crystallizes in the form of individual thin nanowires decorating the whole GO surface. These GO-AgBTC composites can then be used as precursors to prepare small (10 nm) and well-dispersed silver nanoparticles incorporated onto a reduced graphene oxide surface via MOF-mediated synthesis. The presence of AgNPs prevented the stacking of rGO during the reduction process, thus improving the electrochemical active surface area of the electrode materials. Trasatti's analysis of the charge storage mechanism offered a 73.66% capacitive charge storage mechanism for rGO@Ag versus the value of 45.24% obtained by the same method for rGO. rGO@Ag material showed an enhanced specific gravimetric capacitance of 151.97 F/g calculated by galvanostatic charge−discharge curves at 0.5 A/g, and 174.11 F/g obtained by cyclic voltammetry at the scan rate of 2 mV/s. From these results, MOF-mediated synthesis represents an alternative and efficient method to generate nanoparticles decorated graphene electrodes for their application in energy storage field.

■ ASSOCIATED CONTENT

Supporting Information

The Supporting Information is available free of charge at https://pubs.acs.org/doi/10.1021/acsaem.2c03872.

Additional SEM/TEM images and elemental distribution mappings for rGO@Ag; XPS spectra for GO, rGO, and GO-AgBTC; CV curves and specific gravimetric capacitances for rGO@Ag, GO, AgBTC, and GO-AgBTC; comparisons between rGO@Ag and other AgNPs-doped rGO described in literature (PDF)

■ AUTHOR INFORMATION

Corresponding Authors

Enrique Giménez − *Instituto de Tecnología de Materiales, Universitat Politècnica de València (UPV), 46022 Valencia, Spain;* orcid.org/0000-0002-6330-0209; Email: enrique.gimenez@mcm.upv.es

Francesc X. Llabrés i Xamena − *Instituto de Tecnología Química, Universitat Politècnica de València−Consejo Superior de Investigaciones Científicas (UPV-CSIC), Valencia 46022, Spain;* orcid.org/0000-0002-4238-5784; Email: fllabres@itq.upv.es

Authors

Arturo Barjola − *Instituto de Tecnología de Materiales, Universitat Politècnica de València (UPV), 46022 Valencia, Spain*

Anastasia Rapeyko − *Instituto de Tecnología Química, Universitat Politècnica de València−Consejo Superior de Investigaciones Científicas (UPV-CSIC), Valencia 46022, Spain*

https://doi.org/10.1021/acsaem.2c03872
ACS Appl. Energy Mater. XXXX, XXX, XXX−XXX

Oscar Sahuquillo − *Instituto de Tecnología de Materiales, Universitat Politècnica de València (UPV), 46022 Valencia, Spain*

Complete contact information is available at: https://pubs.acs.org/10.1021/acsaem.2c03872

Notes

The authors declare no competing financial interest.

■ ACKNOWLEDGMENTS

The authors are grateful for Grant PID2020-112590GB-C21 funded by MCIN/AEI/10.13039/501100011033.

■ REFERENCES

(1) Pang, H.; Li, X.; Zhao, Q.; Xue, H.; Lai, W. Y.; Hu, Z.; Huang, W. One-Pot Synthesis of Heterogeneous Co3O4-Nanocube/Co-(OH)2-Nanosheet Hybrids for High-Performance Flexible Asymmetric All-Solid-State Supercapacitors. *Nano Energy* **2017**, *35*, 138−145.

(2) Wei, J.; Li, X.; Xue, H.; Shao, J.; Zhu, R.; Pang, H. Hollow Structural Transition Metal Oxide for Advanced Supercapacitors. *Adv. Mater. Interfaces* **2018**, *5* (9), 1701509.

(3) Chen, J.; Li, C.; Shi, G. Graphene Materials for Electrochemical Capacitors. *J. Phys. Chem. Lett.* **2013**, *4* (8), 1244−1253.

(4) Wang, Y.; Shi, Z.; Huang, Y.; Ma, Y.; Wang, C.; Chen, M.; Chen, Y. Supercapacitor Devices Based on Graphene Materials. *J. Phys. Chem. C* **2009**, *113* (30), 13103−13107.

(5) Miller, J. R.; Simon, P. Materials Science: Electrochemical Capacitors for Energy Management. *Science (1979)* **2008**, *321* (5889), 651−652.

(6) Simon, P.; Gogotsi, Y. Materials for Electrochemical Capacitors. *Nature Materials 2008 7:11* **2008**, *7* (11), 845−854.

(7) Huang, L.; Santiago, D.; Loyselle, P.; Dai, L. Graphene-Based Nanomaterials for Flexible and Wearable Supercapacitors. *Small* **2018**, *14* (43), 1800879.

(8) Ruiz, V.; Blanco, C.; Raymundo-Piñero, E.; Khomenko, V.; Béguin, F.; Santamaría, R. Effects of Thermal Treatment of Activated Carbon on the Electrochemical Behaviour in Supercapacitors. *Electrochim. Acta* **2007**, *52* (15), 4969−4973.

(9) Yang, J.; Xiong, P.; Zheng, C.; Qiu, H.; Wei, M. Metal-Organic Frameworks: A New Promising Class of Materials for a High Performance Supercapacitor Electrode. *J. Mater. Chem. A Mater.* **2014**, *2* (39), 16640−16644.

(10) Jung, J.; Kim, D. H. W18O49 Nanowires Assembled on Carbon Felt for Application to Supercapacitors. *Appl. Surf. Sci.* **2018**, *433*, 750−755.

(11) Simon, P.; Gogotsi, Y.; Dunn, B. Where Do Batteries End and Supercapacitors Begin? *Science* **2014**, *343* (6176), 1210−1211.

(12) Zhang, L.; Shi, D.; Liu, T.; Jaroniec, M.; Yu, J. Nickel-Based Materials for Supercapacitors. *Mater. Today* **2019**, *25*, 35−65.

(13) Rahmanifar, M. S.; Hesari, H.; Noori, A.; Masoomi, M. Y.; Morsali, A.; Mousavi, M. F. A Dual Ni/Co-MOF-Reduced Graphene Oxide Nanocomposite as a High Performance Supercapacitor Electrode Material. *Electrochim. Acta* **2018**, *275*, 76−86.

(14) Gao, Y. P.; Huang, K. J. NiCo2S4Materials for Supercapacitor Applications. *Chem. Asian J.* **2017**, *12* (16), 1969−1984.

(15) Li, J. G.; Ho, Y. F.; Ahmed, M. M. M.; Liang, H. C.; Kuo, S. W. Mesoporous Carbons Templated by PEO-PCL Block Copolymers as Electrode Materials for Supercapacitors. *Chem.—Eur. J.* **2019**, *25* (44), 10456−10463.

(16) Tamaddoni Saray, M.; Hosseini, H. Mesoporous MnNiCoO4@MnO2 Core-Shell Nanowire/Nanosheet Arrays on Flexible Carbon Cloth for High-Performance Supercapacitors. *Electrochim. Acta* **2016**, *222*, 505−517.

(17) Wang, S.; Tristan, F.; Minami, D.; Fujimori, T.; Cruz-Silva, R.; Terrones, M.; Takeuchi, K.; Teshima, K.; Rodríguez-Reinoso, F.; Endo, M.; Kaneko, K. Activation Routes for High Surface Area Graphene Monoliths from Graphene Oxide Colloids. *Carbon N Y* **2014**, *76*, 220−231.

(18) Chen, Z.; Ren, W.; Gao, L.; Liu, B.; Pei, S.; Cheng, H. M. Three-Dimensional Flexible and Conductive Interconnected Graphene Networks Grown by Chemical Vapour Deposition. *Nature Materials 2011 10:6* **2011**, *10* (6), 424−428.

(19) Pruna, A.; Cárcel, A. C.; Barjola, A.; Benedito, A.; Giménez, E. Tailoring the Performance of Graphene Aerogels for Oil/Organic Solvent Separation by 1-Step Solvothermal Approach. *Nanomaterials 2019, Vol. 9, Page 1077* **2019**, *9* (8), 1077.

(20) Bleda-Martínez, M. J.; Maciá-Agulló, J. A.; Lozano-Castelló, D.; Morallón, E.; Cazorla-Amorós, D.; Linares-Solano, A. Role of Surface Chemistry on Electric Double Layer Capacitance of Carbon Materials. *Carbon N Y* **2005**, *43* (13), 2677−2684.

(21) Pruna, A. I.; Barjola, A.; Cárcel, A. C.; Alonso, B.; Giménez, E. Effect of Varying Amine Functionalities on CO2 Capture of Carboxylated Graphene Oxide-Based Cryogels. *Nanomaterials 2020, Vol. 10, Page 1446* **2020**, *10* (8), 1446.

(22) Song, Z.; Liu, W.; Xiao, P.; Zhao, Z.; Liu, G.; Qiu, J. Nano-Iron Oxide (Fe2O3)/Three-Dimensional Graphene Aerogel Composite as Supercapacitor Electrode Materials with Extremely Wide Working Potential Window. *Mater. Lett.* **2015**, *145*, 44−47.

(23) Chen, T. T.; Song, W. L.; Fan, L. Z. Engineering Graphene Aerogels with Porous Carbon of Large Surface Area for Flexible All-Solid-State Supercapacitors. *Electrochim. Acta* **2015**, *165*, 92−97.

(24) Ghosh, K.; Yue, C. Y. Development of 3D MoO3/Graphene Aerogel and Sandwich-Type Polyaniline Decorated Porous MnO2-graphene Hybrid Film Based High Performance All-Solid-State Asymmetric Supercapacitors. *Electrochim. Acta* **2018**, *276*, 47−63.

(25) Wu, Z.-S.; Sun, Y.; Tan, Y.-Z.; Yang, S.; Feng, X.; Müllen, K. Three-Dimensional Graphene-Based Macro- and Mesoporous Frameworks for High-Performance Electrochemical Capacitive Energy Storage. *J. Am. Chem. Soc.* **2012**, *134* (48), 19532−19535.

(26) Tingting, Y.; Ruiyi, L.; Xiaohuan, L.; Zaijun, L.; Zhiguo, G.; Guangli, W.; Junkang, L. Nitrogen and Sulphur-Functionalized Multiple Graphene Aerogel for Supercapacitors with Excellent Electrochemical Performance. *Electrochim. Acta* **2016**, *187*, 143−152.

(27) Li, H.; Eddaoudi, M.; O'Keeffe, M.; Yaghi, O. M. Design and Synthesis of an Exceptionally Stable and Highly Porous Metal-Organic Framework. *Nature 1999 402:6759* **1999**, *402* (6759), 276−279.

(28) Zhao, D.; Timmons, D. J.; Yuan, D.; Zhou, H.-C. Tuning the Topology and Functionality of Metal-Organic Frameworks by Ligand Design. *Acc. Chem. Res.* **2011**, *44* (2), 123−133.

(29) Murray, L. J.; Dinca, M.; Long, J. R. Hydrogen Storage in Metal-Organic Frameworks. *Chem. Soc. Rev.* **2009**, *38* (5), 1294−1314.

(30) Rodenas, T.; Luz, I.; Prieto, G.; Seoane, B.; Miro, H.; Corma, A.; Kapteijn, F.; Llabrés i Xamena, F. X.; Gascon, J. Metal-Organic Framework Nanosheets in Polymer Composite Materials for Gas Separation. *Nat. Mater.* **2015**, *14* (1), 48.

(31) Barjola, A.; Reyes-Rodriguez, J. L.; Solorza-Feria, O.; Gimenez, E.; Compan, V. Novel SPEEK-ZIF-67 Proton Exchange Nanocomposite Membrane for PEMFC Application at Intermediate Temperatures. *Ind. Eng. Chem. Res.* **2021**, *60* (25), 9107−9118.

(32) Barjola, A.; Escorihuela, J.; Andrio, A.; Giménez, E.; Compañ, V. Enhanced Conductivity of Composite Membranes Based on Sulfonated Poly(Ether Ether Ketone) (SPEEK) with Zeolitic Imidazolate Frameworks (ZIFs). *Nanomaterials 2018, Vol. 8, Page 1042* **2018**, *8* (12), 1042.

(33) Rogge, S. M. J.; Bavykina, A.; Hajek, J.; Garcia, H.; Olivos-Suarez, A. I.; Sepúlveda-Escribano, A.; Vimont, A.; Clet, G.; Bazin, P.; Kapteijn, F.; Daturi, M.; Ramos Fernandez, E. v; Llabrés i Xamena, F. X.; van Speybroeck, V.; Gascon, J. Metal-Organic and Covalent Organic Frameworks as Single-Site Catalysts. *Chem. Soc. Rev.* **2017**, *46*, 3134−3184.

(34) Gascon, J.; Corma, A.; Kapteijn, F.; Llabrés i Xamena, F. Metal Organic Framework Catalysis: *Quo Vadis*? *ACS Catal.* **2014**, *4* (2), 361−378.

(35) Corma, A.; Garcia, H.; Llabrés i Xamena, F. Engineering Metal Organic Frameworks for Heterogeneous Catalysis. *Chem. Rev.* **2010**, *110* (8), 4606−4655.
(36) Kreno, L. E.; Leong, K.; Farha, O. K.; Allendorf, M. D.; van Duyne, R. P.; Hupp, J. T. Metal Organic Framework Materials as Chemical Sensors. *Chem. Rev.* **2012**, *112*, 1105−1125.
(37) Liang, Z.; Qu, C.; Guo, W.; Zou, R.; Xu, Q. Pristine Metal-Organic Frameworks and Their Composites for Energy Storage and Conversion. *Adv. Mater.* **2018**, *30* (37), 1702891.
(38) Morozan, A.; Jaouen, F. Metal Organic Frameworks for Electrochemical Applications. *Energy Environ. Sci.* **2012**, *5* (11), 9269−9290.
(39) Liu, X.; Shi, C.; Zhai, C.; Cheng, M.; Liu, Q.; Wang, G. Cobalt-Based Layered Metal-Organic Framework as an Ultrahigh Capacity Supercapacitor Electrode Material. *ACS Appl. Mater. Interfaces* **2016**, *8* (7), 4585−4591.
(40) Choi, K. M.; Jeong, H. M.; Park, J. H.; Zhang, Y. B.; Kang, J. K.; Yaghi, O. M. Supercapacitors of Nanocrystalline Metal-Organic Frameworks. *ACS Nano* **2014**, *8* (7), 7451−7457.
(41) Liu, Y.; Li, G.; Fu, J.; Chen, Z.; Peng, X. Strings of Porous Carbon Polyhedrons as Self-Standing Cathode Host for High-Energy-Density Lithium-Sulfur Batteries. *Angew. Chem., Int. Ed.* **2017**, *56* (22), 6176−6180.
(42) Xia, W.; Qu, C.; Liang, Z.; Zhao, B.; Dai, S.; Qiu, B.; Jiao, Y.; Zhang, Q.; Huang, X.; Guo, W.; Dang, D.; Zou, R.; Xia, D.; Xu, Q.; Liu, M. High-Performance Energy Storage and Conversion Materials Derived from a Single Metal-Organic Framework/Graphene Aerogel Composite. *Nano Lett.* **2017**, *17* (5), 2788−2795.
(43) Wan, L.; Wei, J.; Liang, Y.; Hu, Y.; Chen, X.; Shamsaei, E.; Ou, R.; Zhang, X.; Wang, H. ZIF-Derived Nitrogen-Doped Carbon/3D Graphene Frameworks for All-Solid-State Supercapacitors. *RSC Adv.* **2016**, *6* (80), 76575−76581.
(44) Wen, P.; Li, Z.; Gong, P.; Sun, J.; Wang, J.; Yang, S. Design and Fabrication of Carbonized RGO/CMOF-5 Hybrids for Supercapacitor Applications. *RSC Adv.* **2016**, *6* (16), 13264−13271.
(45) Inonu, Z.; Keskin, S.; Erkey, C. An Emerging Family of Hybrid Nanomaterials: Metal-Organic Framework/Aerogel Composites. *ACS Appl. Nano Mater.* **2018**, *1* (11), 5959−5980.
(46) Zhang, X.; Sui, Z.; Xu, B.; Yue, S.; Luo, Y.; Zhan, W.; Liu, B. Mechanically Strong and Highly Conductive Graphene Aerogel and Its Use as Electrodes for Electrochemical Power Sources. *J. Mater. Chem.* **2011**, *21* (18), 6494−6497.
(47) Azadfalah, M.; Sedghi, A.; Hosseini, H. Synthesis of Nano-Flower Metal-Organic Framework/Graphene Composites As a High-Performance Electrode Material for Supercapacitors. *J. Electron. Mater.* **2019**, *48* (11), 7011−7024.
(48) Das, R.; Pachfule, P.; Banerjee, R.; Poddar, P. Metal and Metal Oxide Nanoparticle Synthesis from Metal Organic Frameworks (MOFs): Finding the Border of Metal and Metal Oxides. *Nanoscale* **2012**, *4* (2), 591−599.
(49) Cao, X.; Zheng, B.; Rui, X.; Shi, W.; Yan, Q.; Zhang, H. Metal Oxide-Coated Three-Dimensional Graphene Prepared by the Use of Metal-Organic Frameworks as Precursors. *Angew. Chem.* **2014**, *126* (5), 1428−1433.
(50) Guan, B. Y.; Kushima, A.; Yu, L.; Li, S.; Li, J.; Lou, X. W. D. Coordination Polymers Derived General Synthesis of Multishelled Mixed Metal-Oxide Particles for Hybrid Supercapacitors. *Adv. Mater.* **2017**, *29* (17), 1605902.
(51) Wang, R.; Haspel, H.; Pustovarenko, A.; Dikhtiarenko, A.; Russkikh, A.; Shterk, G.; Osadchii, D.; Ould-Chikh, S.; Ma, M.; Smith, W. A.; Takanabe, K.; Kapteijn, F.; Gascon, J. Maximizing Ag Utilization in High-Rate CO2 Electrochemical Reduction with a Coordination Polymer-Mediated Gas Diffusion Electrode. *ACS Energy Lett.* **2019**, *4* (8), 2024−2031.
(52) Zheng, L.; Zhang, G.; Zhang, M.; Guo, S.; Liu, Z. H. Preparation and Capacitance Performance of Ag-Graphene Based Nanocomposite. *J. Power Sources* **2012**, *201*, 376−381.
(53) Lu, L.; Liu, J.; Hu, Y.; Zhang, Y.; Chen, W. Graphene-Stabilized Silver Nanoparticle Electrochemical Electrode for Actuator Design. *Adv. Mater.* **2013**, *25* (9), 1270−1274.
(54) Hsieh, C. te; Lin, C. Y.; Chen, Y. F.; Lin, J. S.; Teng, H. Silver Nanorods Attached to Graphene Sheets as Anode Materials for Lithium-Ion Batteries. *Carbon N Y* **2013**, *62*, 109−116.
(55) Han, X. W.; Guo, S.; Li, T.; Peng, J.; Pan, H. Construction of Ag/3D-Reduced Graphene Oxide Nanocomposite with Advanced Catalytic Capacity for 4-Nitrophenol and Methylene Blue. *Colloids Surf. A Physicochem Eng. Asp* **2022**, *650*, 128688.
(56) Yang, S.; Zhou, Y.; Zhao, Y.; Wang, D.; Luan, Y. Microwave Synthesis of Graphene Oxide Decorated with Silver Nanoparticles for Slow-Release Antibacterial Hydrogel. *Mater. Today Commun.* **2022**, *31*, 103663.
(57) Barjola, A.; Tormo-Mas, M. Á.; Sahuquillo, O.; Bernabé-Quispe, P.; Pérez, J. M.; Giménez, E. Enhanced Antibacterial Activity through Silver Nanoparticles Deposited onto Carboxylated Graphene Oxide Surface. *Nanomaterials (Basel)* **2022**, *12* (12), 1949.
(58) Marcano, D. C.; Kosynkin, D. V.; Berlin, J. M.; Sinitskii, A.; Sun, Z.; Slesarev, A.; Alemany, L. B.; Lu, W.; Tour, J. M. Improved Synthesis of Graphene Oxide. *ACS Nano* **2010**, *4* (8), 4806−4814.
(59) Nowacka, A.; Briantais, P.; Prestipino, C.; Llabrés i Xamena, F. X. Facile "Green" Aqueous Synthesis of Mono- and Bimetallic Trimesate Metal-Organic Frameworks. *ACS Sustainable Chem. Eng.* **2019**, *19* (9), 4981−4989.
(60) Morris, R. E.; Wheatley, P. S.; Warrender, S.; Duncan, M. Synthesis of MOFS. WO Pat.2013186542A1, 2013.
(61) Ferrari, A. C.; Basko, D. M. Raman Spectroscopy as a Versatile Tool for Studying the Properties of Graphene. *Nature Nanotechnology 2013 8:4* **2013**, *8* (4), 235−246.
(62) Jain, A.; Ghosh, M.; Krajewski, M.; Kurungot, S.; Michalska, M. Biomass-Derived Activated Carbon Material from Native European Deciduous Trees as an Inexpensive and Sustainable Energy Material for Supercapacitor Application. *J. Energy Storage* **2021**, *34*, 102178.
(63) Bello, A.; Fabiane, M.; Dodoo-Arhin, D.; Ozoemena, K. I.; Manyala, N. Silver Nanoparticles Decorated on a Three-Dimensional Graphene Scaffold for Electrochemical Applications. *J. Phys. Chem. Solids* **2014**, *75* (1), 109−114.
(64) Zhao, L.; Yang, S. T.; Feng, S.; Ma, Q.; Peng, X.; Wu, D. Preparation and Application of Carboxylated Graphene Oxide Sponge in Dye Removal. *International Journal of Environmental Research and Public Health 2017, Vol. 14, Page 1301* **2017**, *14* (11), 1301.
(65) Jain, A.; Tripathi, S. K. Nano-Porous Activated Carbon from Sugarcane Waste for Supercapacitor Application. *J. Energy Storage* **2015**, *4*, 121−127.
(66) Shen, J.; Hu, Y.; Shi, M.; Lu, X.; Qin, C.; Li, C.; Ye, M. Fast and Facile Preparation of Graphene Oxide and Reduced Graphene Oxide Nanoplatelets. *Chem. Mater.* **2009**, *21* (15), 3514−3520.
(67) Biswas, M. C.; Tiimob, B. J.; Abdela, W.; Jeelani, S.; Rangari, V. K. Nano Silica-Carbon-Silver Ternary Hybrid Induced Antimicrobial Composite Films for Food Packaging Application. *Food Packag Shelf Life* **2019**, *19*, 104−113.
(68) Wu, Y.; Guan, F.; Li, X.; Gong, Y.; Wang, X.; Zhou, J.; Chen, Y. Thermoresistant Hybrid Ag/RGO Fiber Supercapacitors. *Fibers Polym.* **2022**, *23* (3), 626−635.
(69) Liu, Y.; Tian, C.; Yan, B.; Lu, Q.; Xie, Y.; Chen, J.; Gupta, R.; Xu, Z.; Kuznicki, S. M.; Liu, Q.; Zeng, H. Nanocomposites of Graphene Oxide, Ag Nanoparticles, and Magnetic Ferrite Nanoparticles for Elemental Mercury (Hg0) Removal. *RSC Adv.* **2015**, *5* (20), 15634−15640.
(70) Gunawan, C.; Teoh, W. Y.; Marquis, C. P.; Lifia, J.; Amal, R. Reversible Antimicrobial Photoswitching in Nanosilver. *Small* **2009**, *5* (3), 341−344.
(71) Raymundo-Piñero, E.; Cadek, M.; Béguin, F. Tuning Carbon Materials for Supercapacitors by Direct Pyrolysis of Seaweeds. *Adv. Funct Mater.* **2009**, *19* (7), 1032−1039.
(72) Schoetz, T.; Gordon, L. W.; Ivanov, S.; Bund, A.; Mandler, D.; Messinger, R. J. Disentangling Faradaic, Pseudocapacitive, and Capacitive Charge Storage: A Tutorial for the Characterization of

https://doi.org/10.1021/acsaem.2c03872
ACS Appl. Energy Mater. XXXX, XXX, XXX−XXX

Batteries, Supercapacitors, and Hybrid Systems. *Electrochim. Acta* **2022**, *412*, 140072.
(73) Ardizzone, S.; Fregonara, G.; Trasatti, S. Inner" and "Outer" Active Surface of RuO2 Electrodes. *Electrochim. Acta* **1990**, *35* (1), 263−267.
(74) Augustyn, V.; Come, J.; Lowe, M. A.; Kim, J. W.; Taberna, P. L.; Tolbert, S. H.; Abruña, H. D.; Simon, P.; Dunn, B. High-Rate Electrochemical Energy Storage through Li+ Intercalation Pseudocapacitance. *Nature Materials 2013 12:6* **2013**, *12* (6), 518−522.
(75) Le, Z.; Liu, F.; Nie, P.; Li, X.; Liu, X.; Bian, Z.; Chen, G.; Wu, H. B.; Lu, Y. Pseudocapacitive Sodium Storage in Mesoporous Single-Crystal-like TiO2-Graphene Nanocomposite Enables High-Performance Sodium-Ion Capacitors. *ACS Nano* **2017**, *11* (3), 2952−2960.

https://doi.org/10.1021/acsaem.2c03872
ACS Appl. Energy Mater. XXXX, XXX, XXX−XXX